RSC Advances

PAPER

View Article Online
View Journal | View Issue

Cite this: *RSC Adv.*, 2026, **16**, 4062

Enhanced removal of crystal violet from aqueous solutions using $BaTiO_3$@ZnO: isotherm, kinetic, and thermodynamic evaluation

Ahmed Barakat,[a] Magdi E. Khalifa,[a] A. M. Abdelghany[bc] and Wael I. Mortada *[d]

Crystal violet (CV), commonly utilized in various industries, presents risks to both the environment and human health because of its durability and harmful nature. This research discusses the synthesis of a $BaTiO_3$@ZnO composite for effectively eliminating CV from aqueous solutions. The composite was produced through a solid-state technique and characterized using XRD, FTIR, SEM-EDX, TEM, BET, and pH_{pzc}. The study of CV adsorption involves optimizing various parameters that influence the process, including pH, initial dye concentration, dosage of the adsorbent, contact time, temperature, and ionic strength. The $BaTiO_3$@ZnO composite displayed a mesoporous configuration with a surface area of 34.1 $m^2\ g^{-1}$, a total pore volume of 0.0354 $cm^3\ g^{-1}$, and an average pore radius of 2.53 nm, along with an average crystallite size of 64.58 nm. The experimental data align most closely with the Langmuir isotherm and pseudo-second-order kinetic model, indicating that monolayer adsorption and chemisorption are the main processes involved. The Langmuir isotherm demonstrated a maximum monolayer adsorption capacity of 97.84 mg g^{-1} for the $BaTiO_3$@ZnO composite. The thermodynamic studies suggest that the adsorption processes are spontaneous and endothermic. The $BaTiO_3$@ZnO composite can be effectively recycled and reused for up to ten cycles, maintaining relatively high adsorption capacity despite a gradual decline over successive cycles. This study exhibited the success of doping ZnO into $BaTiO_3$ to form a composite that possesses enhanced surface area, porosity, and surface charge, thereby making the $BaTiO_3$@ZnO composite a promising and efficient adsorbent for CV removal in industrial wastewater.

Received 8th December 2025
Accepted 14th January 2026

DOI: 10.1039/d5ra09495j

rsc.li/rsc-advances

1. Introduction

Water contaminated with organic dyes is a major environmental issue, especially given the extensive application of dyes across multiple industries.[1] Textiles, leather, paper, plastics, and other industrial fields extensively use organic dyes to add brilliant color to their products.[2] Organic dyes are one of the toxic pollutants that cause serious environmental and health hazards due to their recalcitrance to biodegradation and conventional approaches for wastewater treatment. When organic dyes discharge into water bodies, they cause a harmful effect on the aquatic systems.[3]

Crystal violet (CV), a synthetic cationic dye and a member of the triphenylmethane group, is widely employed in textile dyeing, printing, veterinary medicine, dermatology, forensic science, and cosmetics.[4] Unfortunately, CV poses severe health risks; it has carcinogenic and mutagenic effects.[5] Prolonged exposure to CV may create problems with the liver and kidneys. In addition, CV is irritating to the skin, causes nausea and vomiting, may affect the respiratory system, and damages the cornea and conjunctiva.[6] If a CV is released into a natural water system, it must be removed from wastewater before discharge.

Various approaches are employed to remove organic dyes from wastewater. These procedures include coagulation, flocculation,[7] electrochemical methods,[8,9] advanced oxidation processes,[10] membrane filtration,[11] biodegradation,[12] and adsorption.[13,14] Among these techniques, adsorption is the best choice. It is easy to use, low-cost, and highly effective at removing dyes even in low concentrations. The adsorbent can be regenerated and reused several times, reflecting its eco-friendliness and economic impacts. The effectiveness of an adsorbent depends on its surface area, porosity, and surface chemistry.

Traditional adsorbent materials may suffer from drawbacks such as being expensive, difficult to regenerate, or effective only under certain conditions.[15] Metal oxides such as ZnO, TiO_2, Fe_3O_4, and $BaTiO_3$ are extensively investigated as adsorbents and catalysts because of their stability, non-toxicity, availability, and ability to operate under varied pH and temperature conditions. These materials are expected to overcome the

[a]*Chemistry Department, Faculty of Science, Mansoura University, Mansoura 35516, Egypt*
[b]*Spectroscopy Department, Physics Research Institute, National Research Centre, Giza, 12311, Egypt*
[c]*Basic and Applied Science Department, Horus University, International Coastal Rd, Kafr Saad, New Damietta, 34511, Egypt*
[d]*Urology and Nephrology Center, Mansoura University, Mansoura 35516, Egypt. E-mail: w.mortada@mans.edu.eg*

limitations of traditional adsorbents by offering a high adsorption capacity, fast kinetics, and reusability, thereby contributing to sustainable wastewater treatment solutions.[16]

There are various plans to improve the adsorption capacity of $BaTiO_3$, for example, modifying the size and morphology of $BaTiO_3$ particles through the temperature of synthesis and reaction periods, doping with noble metal nanoparticles (Ag and Au), and creating composites with other semiconductors (ZnO and TiO_2) or carbon-based material ($BaTiO_3$@graphene).[17] The $BaTiO_3$@ZnO composite has an antimicrobial activity.[18] In addition to environmental applications, $BaTiO_3$@ZnO composites have been investigated for electronic devices and energy storage applications.[19] These different applications point out the composite's potential as a multipurpose material for sustainable and innovative technologies.

The objective of this work is to investigate the efficiency of $BaTiO_3$@ZnO composite as an adsorbent for CV removal from its aqueous solutions. $BaTiO_3$@ZnO has stable physicochemical properties, low cost, reusability, and environmental friendliness. For this aim, $BaTiO_3$ was modified with zinc oxide (ZnO) to form a composite material ($BaTiO_3$@ZnO). ZnO enhances the surface characteristics of the composite by increasing the specific surface area, improving porosity, and giving more active adsorption sites. Furthermore, ZnO offers a high isoelectric point and supports electrostatic interactions with aromatic dye molecules. The composite has a synergistic effect that improves the adsorption capacity. The $BaTiO_3$@ZnO composite was easily synthesized by a solid-state technique, which is environmentally friendly and does not use hazardous solvents or toxic chemicals. X-ray diffraction (XRD), Fourier transform infrared (FTIR), scanning electron microscopy (SEM), transmission electron microscopy (TEM), and Brunauer–Emmett–Teller (BET) were employed to characterize the composite to establish a relationship between structural and surface characteristics of the composite and adsorption capacity. The effects of parameters (pH, initial dye concentration, adsorbent dosage, contact time, temperature, and ionic strength) on the adsorption process were investigated. Kinetics, thermodynamics, and adsorption isotherms were studied to understand the CV adsorption mechanism.

2. Experimental

2.1. Chemicals

In this study, analytical-grade chemicals and distilled water were employed. Anatase titanium dioxide (TiO_2; purity of 99.8%), zinc oxide (ZnO; purity of 99.8%), and barium carbonate ($BaCO_3$; purity of 99.9%) were purchased from Sigma-Aldrich (St. Louis, MO, USA). CV dye obtained from (Merck, Darmstadt, Germany). Analytical grade HCl (37%, El-Gomhouria, Egypt) and NaOH (≥98%, analytical grade, El-Gomhouria, Egypt) were used to adjust the pH of solutions.

2.2. Stock solution of CV

A 1000 mg L^{-1} stock solution of CV dye was prepared by dissolving 1.0 g of CV in 1000 mL of distilled water. UV-Vis spectrophotometry analysis revealed the wavelength of maximum absorption to be 590 nm. Working solutions were prepared daily by dilution of the stock solution.

2.3. Synthesis of $BaTiO_3$@ZnO composite

The $BaTiO_3$@ZnO composite was produced *via* a single-step solid-state reaction route.[20,21] In a typical preparation, 2.35 g of barium carbonate ($BaCO_3$), 1.60 g of titanium dioxide (TiO_2), and 0.81 g of zinc oxide (ZnO) were weighed according to the desired stoichiometric ratio. The powders were thoroughly mixed in an agate mortar and subjected to ball milling for 2 h. The homogenized mixture was placed in a platinum crucible and underwent a thermal treatment program that involved 2 hours at 350 °C to eliminate carbon dioxide from the decomposition of $BaCO_3$, followed by 6 hours at 1000 °C. This technique introduces simplicity, scalability, and cost-effectiveness.

2.4. Instrumentation

The $BaTiO_3$@ZnO composite was characterized using a range of analytical instruments. XRD was performed with a Bruker D8 advanced X-ray diffractometer (Germany) using a monochromatic Cu-Kα radiation source, $\lambda = 0.15406$ nm, running at 40 kV. FTIR spectra were recorded in the 4000–400 cm^{-1} regions at a resolution of 2 cm^{-1} on a Nicolet FTIR spectrophotometer (model 6700, USA) employing the KBr disk method. SEM images were obtained through Jeol JSM-6510LV equipment (Japan) equipped with energy dispersive X-ray (EDX), while TEM images were captured using a Jeol JEM-2100 instrument (Japan). The surface area was assessed *via* the BET method using the N_2 adsorption/desorption technique (NOVA Touch 4LX analyzer, USA). The CV concentrations were analyzed by a UV-Vis spectrophotometer (Unico Model 1200, USA) at a wavelength of 590 nm. The pH levels of the solutions were assessed by a pH meter (Adwa AD1030, China). A rotary orbital shaker (BIBBY Stuart Scientific-SO1, UK) was utilized for batch experiments. A centrifuge (80–2 electric, China) was also employed in the experiments to facilitate phase separation.

2.5. pHpzc

The point of zero charge (pH_{PZC}) of the $BaTiO_3$@ZnO composite was determined through the pH drift method. In this method, a series of 50 mL NaCl solutions (0.1 mol L^{-1}) was adapted to a pH range (2–10) using NaOH (0.1 mol L^{-1}) and HCl (0.1 mol L^{-1}), followed by adding 20 mg of $BaTiO_3$@ZnO composite in each tube and agitating at 200 rpm. After 24 h, the composite was extracted from the solution, and finally, the pH of the solutions was determined again. The difference between the initial and final pH (ΔpH) was plotted *versus* initial pH to estimate pHpzc, which is the point when ΔpH equals zero.

2.6. Batch adsorption experiments of $BaTiO_3$ and $BaTiO_3$@ZnO

Batch adsorption tests were executed to assess the influences of experimental factors on CV removal using $BaTiO_3$ and $BaTiO_3$@ZnO composite. The goal of studying $BaTiO_3$, besides the $BaTiO_3$@ZnO composite, was to compare the performance and adsorption behavior of both adsorbents. The investigated

factors included pH (2–10), adsorbent dose (5–70 mg), initial dye concentration (30–200 mg L^{-1}), contact time (30–390 min), temperature (25–50 °C), and ionic strength (0.05–0.25 mol L^{-1} of NaCl). In a standard experiment, a known quantity of adsorbent was added to 10 mL of CV solution at the desired pH. The mixture was stirred at 200 rpm at room temperature using a rotary shaker until equilibrium was reached, which occurred after 300 min for $BaTiO_3$ and 360 min for the $BaTiO_3$@ZnO composite. After reaching equilibrium, the samples were centrifuged for 15 min at 4000 rpm to extract the adsorbent from the solution. The CV concentration in the supernatant was then measured by a spectrophotometer at 590 nm.

Eqn (1) and (2) were used to estimate the amount of CV adsorbed at equilibrium (q_e) (mg g^{-1}) and the percentage of CV removal (%E), respectively:

$$q_e = \frac{(C_0 - C_e)V}{m} \quad (1)$$

$$\% E = \frac{C_0 - C_e}{C_0} \times 100 \quad (2)$$

where C_0 (mg L^{-1}) is the initial CV concentration, C_e (mg L^{-1}) is the equilibrium concentration of CV, V (L) is the volume of CV solution, and m (g) is the mass of the adsorbent.

Table 1 Characteristic of environmental water samples

Nile river water		Sewage wastewater	
TDS	315 mg L^{-1}	TDS	1005 mg L^{-1}
Turbidity (NTU)	15.24 NTU	TSS	19 mg L^{-1}
BOD	10.0 mg L^{-1}	BOD	52 mg L^{-1}
COD	6.0 mg L^{-1}	COD	66 mg L^{-1}
DO	6.27 mg L^{-1}	DO	6.4 mg L^{-1}
NO_2	0.53 mg L^{-1}	NO_2	25 mg L^{-1}
NO_3	3.2 mg L^{-1}	NO_3	0.3 mg L^{-1}
PO_4	0.96 mg L^{-1}	PO_4	3.2 mg L^{-1}
NH_3–N	0.03 mg L^{-1}	NH_3–N	3 mg L^{-1}

2.7. Desorption and reusability

Desorption and reusability were studied to evaluate the economic benefit and practical application of $BaTiO_3$ and $BaTiO_3$@ZnO composite adsorbents for the removal of CV. Ten successive adsorption–desorption cycles were carried out under fixed conditions (initial dye concentration: 50 mg L^{-1}, adsorbent dose: 10 mg, volume: 10 mL, temperature: 35 °C, equilibrium time: 360 min, pH: 8). After each cycle, dye molecules were desorbed from the adsorbents using absolute ethanol, followed by rinsing with deionized water and drying at 70 °C for 1 h before reuse again.

2.8. Application

Two real water samples (Table 1) and one synthetic effluent sample were used to test the applicability of the procedure for the recovery of CV. Samples from the Nile River (Mansoura) and Sewage wastewater were collected and centrifuged at 4000 rpm for 10 min to remove any suspended particles. The supernatants were separated and subjected to the recovery procedure. A synthetic effluent sample was prepared according to Li *et al.*[22] 10 mg each of NaCl, Na_2SO_4, CH_3COONa, Na_2CO_3, Na_2HPO_4, $MgSO_4$, $CaCl_2$, and KCl were dissolved separately and mixed to form 1.0 L of the synthetic sample. 10 mL of each sample was spiked with different concentrations of CV and subjected to the optimized procedure. A simple diagram illustrating the workflow and apparatus for the real-sample adsorption tests is shown in Fig. (1). The recovery was calculated from the following relation:

$$R = \frac{\text{Concentration spiked} - \text{Concentration unspiked}}{\text{Concentration added}} \times 100 \quad (3)$$

3. Results and discussion

3.1. Characterization of $BaTiO_3$@ZnO composite

3.1.1. XRD. X-ray diffraction (XRD) analysis is an essential technique for examining the crystalline structure, phase

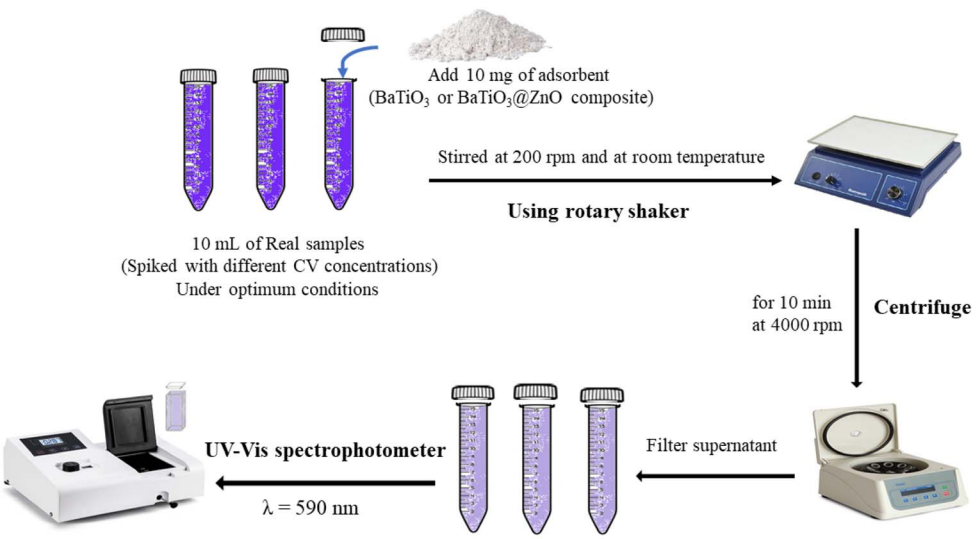

Fig. 1 Workflow diagram for the real-sample adsorption tests.

composition, and average particle size of the $BaTiO_3$@ZnO composite. The XRD pattern of the $BaTiO_3$@ZnO composite before and after CV adsorption is displayed in Fig. 2a.

As shown in pattern (2a I), before CV adsorption, it illustrates the crystalline phases corresponding to the two components: $BaTiO_3$ and ZnO. The major diffraction peaks observed at 2θ = 31.7°, 34.4°, 36.2°, 47.5°, 56.5°, 62.8°, 66.3°, 67.9°, 69.02°, 72.5°, and 76.9° with corresponding planes (100), (002), (101), (102), (110), (103), (200), (112), (201), (004), and (202), respectively, are characteristic of the hexagonal wurtzite structure of ZnO, which matched with standard reference patterns (JCPDS No. 36-1451).[23] This confirms the presence of ZnO with a hexagonal structure, lattice parameters $a = b = 3.24950$ Å and $c = 5.20690$ Å, and space group P 63 mc. While the diffraction peaks located at 2θ = 25.3°, 37.8°, 38.6°, 48.1°, 53.9°, 55.1°, 62.1°, 62.7°, 70.3°, and 75° are assigned to planes (101), (004), (112), (200), (105), (211), (213), (204), (220), and (215), respectively, they are related to anatase phases of TiO_2 (JCPDS No. 21-1272).[24] This confirms the presence of a tetragonal $BaTiO_3$ structure with lattice parameters $a = b = 3.785$ Å and $c = 9.514$ Å and the $I4_1/amd$ space group. The XRD spectra indicate the successful formation of the $BaTiO_3$@ZnO composite. The average crystallite size of the particles can be determined using the Debye–Scherrer formula (3).

$$D = \frac{k\lambda}{\beta\cos\theta} \quad (4)$$

where D is the average crystallite size (nm), k is a constant (shape factor around 0.9), λ corresponds to the wavelength of the X-ray applied (0.15406 nm), β is the FWHM (full width at half maximum) of the diffraction lines, and θ is the Bragg diffraction angle. The average crystallite size of the particles was determined to be 64.58 nm, which is a nanoparticle size and is suitable for the adsorption process.

In pattern (2a II), after CV adsorption, there are changes in some diffraction peaks, marked with asterisks (additional peaks at 2θ = 27.8° and 59.1° – peak intensity at 2θ = 23.9°, 42.0°, 43.0°, 44.9°, and 46.7°). These peaks may be ascribed to the interaction of CV with the composite surface. The crystalline peaks of the $BaTiO_3$@ZnO composite remain the same with no change, indicating the integrity of the $BaTiO_3$@ZnO composite and the ability to reuse it in dye removal.

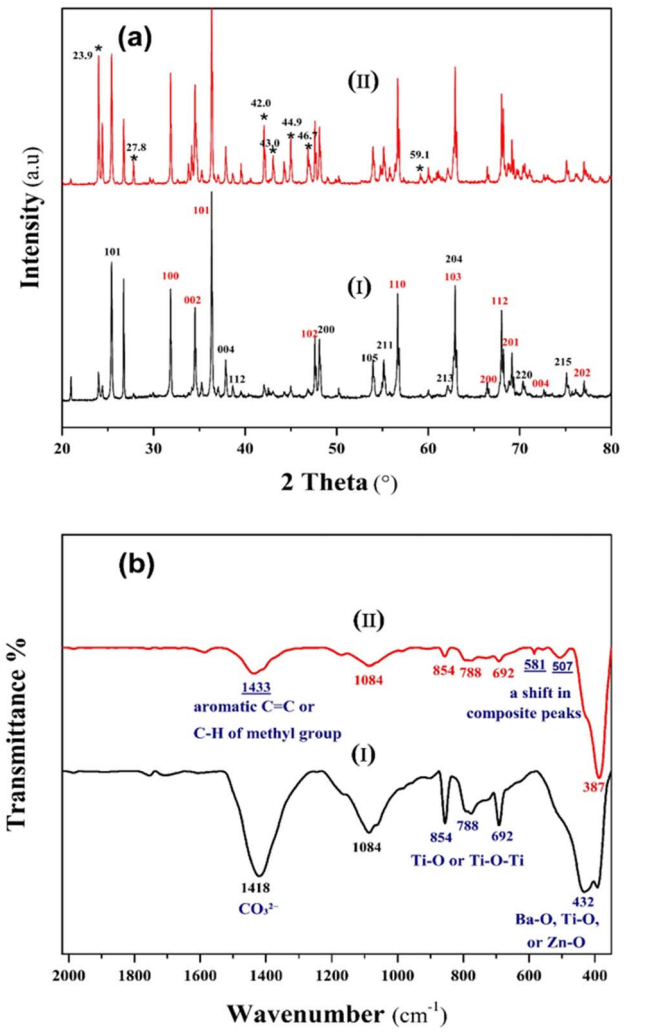

Fig. 2 (a) XRD pattern of $BaTiO_3$@ZnO composite: (I) before and (II) after adsorption of CV; (b) FTIR spectra of $BaTiO_3$@ZnO composite: (I) before and (II) after adsorption of CV.

3.1.2. FTIR. Fourier-transform infrared (FTIR) spectroscopy was employed to identify the functional groups present on the surface of the $BaTiO_3$@ZnO composite and to investigate the nature of interactions with CV dye. The spectra recorded before and after CV adsorption are displayed in Fig. 2b. Before adsorption (spectrum I), the composite exhibits characteristic bands at 432 cm^{-1}, attributable to stretching vibrations of Ba–O, Ti–O, and/or Zn–O bonds.[25–27] Additional peaks at 692, 788, and 854 cm^{-1} are associated with Ti–O and Ti–O–Ti stretching modes,[28] confirming the formation of the $BaTiO_3$ phase. A sharp band near 1418 cm^{-1} corresponds to residual carbonate (CO_3^{2-}) vibrations,[29] likely originating from the $BaCO_3$ precursor.

After CV adsorption (spectrum II), several changes are observed. A new band emerges at 1433 cm^{-1}, which can be assigned to aromatic C=C stretching or C–H bending vibrations of the methyl groups in the CV molecule.[30,31] Additionally, shifts and intensity alterations occur in the low-frequency region: a new band appears at 502 cm^{-1}, possibly due to Ti–O or Zn–O bending vibrations,[32,33] while a band at 581 cm^{-1} emerges, corresponding to metal–oxygen stretching modes.[32] Moreover, the intensities of the peaks at 1084 and 854 cm^{-1} decrease noticeably, suggesting surface interactions that modify vibrational modes of the composite. The absence of distinct ZnO-specific bands in the spectrum may be due to the low IR activity of Zn–O vibrations and their overlap with Ba–O and Ti–O modes. Nevertheless, the observed spectral changes before and after adsorption provide strong evidence of interfacial interactions, indicating that CV adsorption involves both electrostatic attraction and chemisorption onto the composite surface.

3.1.3. SEM/EDX analysis. SEM provides important details about the surface morphology of the $BaTiO_3$@ZnO composite as depicted in Fig. 3a. The SEM image exhibits particles agglomerated with irregular shapes and varying sizes. The particles possess a smooth surface with a uniform distribution. The

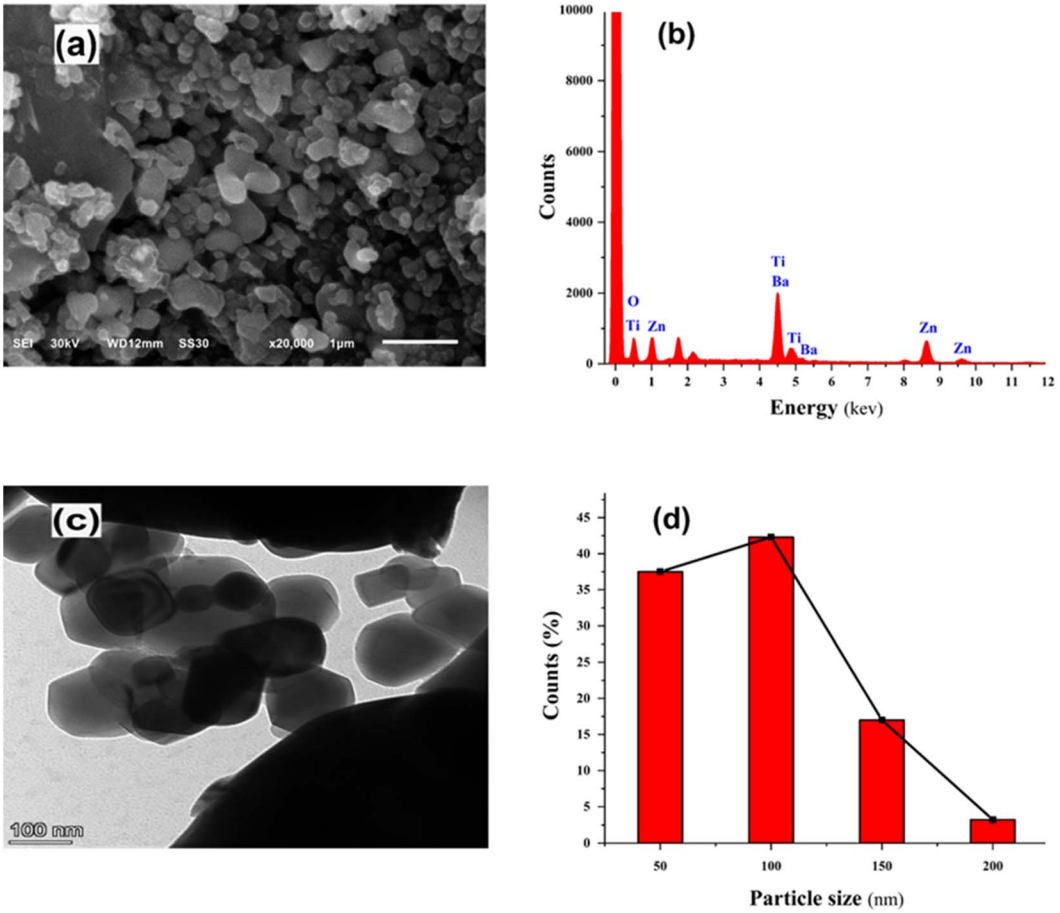

Fig. 3 (a) SEM image; (b) EDX image; (c)TEM image; (d) histogram of particle size distribution: for $BaTiO_3$@ZnO composite.

image shows that the composite is present in a crystalline structure.

Energy dispersive X-ray (EDX) is an analytical technique that determines the elemental components of a sample. The EDX spectrum confirmed the elemental composition of the $BaTiO_3$@-ZnO composite, illustrating Ba, Ti, O, and Zn as the major constituents (Fig. 3b). The percentage mass of elements—barium (2.70%), titanium (9.28%), oxygen (80.28%), and zinc (7.74%)—is displayed in Table 2. This result confirms the successful incorporation of ZnO with $BaTiO_3$ to form a composite.

3.1.4. TEM. The crystalline particle size and distribution of the $BaTiO_3$@ZnO composite are shown in the TEM image (Fig. 3c). The TEM image reveals that the composite consists of nanoparticles mainly spherical to slightly polyhedral in shape with different sizes. The image illustrates an agglomeration of particles with a moderate uniform distribution, which is a common feature in metal oxide nanomaterials synthesized by wet chemical techniques. The corresponding particle size distribution histogram (Fig. 3d), derived from the TEM image, indicates the average particle diameter is 67.95 nm, with the most particles located in the range 50–100 nm. This value matches XRD calculations.

Table 2 EDX analysis of $BaTiO_3$@ZnO composite

Element	Weight %	Atomic %
O	49.29	80.28
Ti	17.05	9.28
Zn	19.41	7.74
Ba	14.24	2.70
Total	100	100

3.1.5. BET studies. The N_2 adsorption–desorption isotherm was carried out to get the surface area and pore characteristics of both the $BaTiO_3$@ZnO composite and $BaTiO_3$.

The $BaTiO_3$@ZnO composite exhibits type IV isotherms according to the IUPAC classification with a hysteresis ring, which indicates a mesoporous structure of the composite, as depicted in Fig. 4a. As illustrated in Table 3, the BET surface area of the $BaTiO_3$@ZnO composite and $BaTiO_3$ were found to be 34.1 $m^2\ g^{-1}$ and 28.1 $m^2\ g^{-1}$, respectively. Average pore radius and pore volume were determined by the Barret-Joyner-Halenda (BJH) method. The average pore radius of the $BaTiO_3$@ZnO composite was 2.53 nm, and for $BaTiO_3$, it was 3.59 nm. Pore volume for the $BaTiO_3$@ZnO composite and $BaTiO_3$ were noticed to be 0.0354 $cm^3\ g^{-1}$ and 0.0437 $cm^3\ g^{-1}$, respectively. Pore size distribution curve using the BJH method (Fig. 4b) indicates that most pores of the composite are centered around 2.5 nm with a uniform mesoporous structure, which is favorable for diffusion and interaction of dye molecules with the active surface.

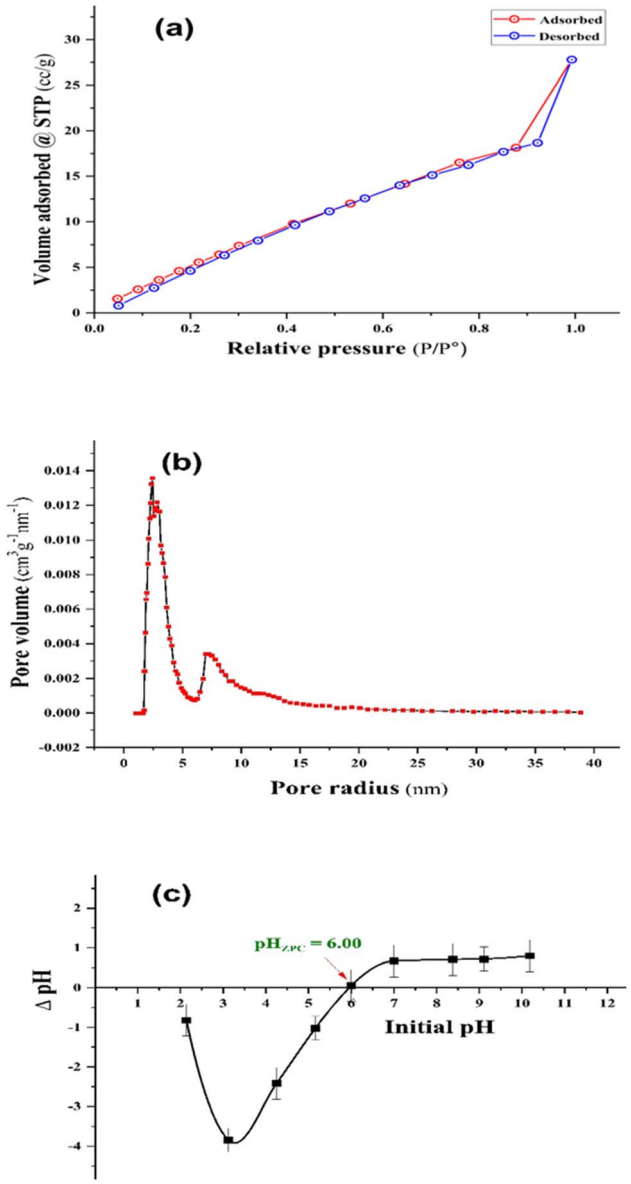

Fig. 4 (a) N_2 adsorption desorption isotherm; (b) BJH plot and pore size distribution; (c) point zero charge (PZC): for $BaTiO_3$@ZnO composite.

The results showed that the $BaTiO_3$@ZnO composite has a higher surface area and has a slight decrease in pore volume and average pore radius to become a finer mesoporous material, making it more efficient for removing CV from wastewater. This matches previous studies that have shown ZnO addition to $BaTiO_3$ increases the specific surface area, decreases particle size, and improves surface morphology and reactivity; all of these contribute to better adsorption of dye molecules.[34]

Table 3 Surface area and pore characteristics of $BaTiO_3$@ZnO composite and $BaTiO_3$

Sample	BET surface area ($m^2\ g^{-1}$)	Pore volume ($cm^3\ g^{-1}$)	Average pore radius (nm)
$BaTiO_3$	28.1	0.0437	3.59
$BaTiO_3$@ZnO	34.1	0.0354	2.53

3.1.6. Point of zero charge. pHpzc is the point at which the adsorbent surface exhibits a neutral net charge. The pHpzc of $BaTiO_3$@ZnO composite was found to be pH 6.0, as displayed in Fig. 4c. This indicates that the composite surface acquires a negative charge above this value and has a positive charge at values below.[35] It is an essential parameter in the electrostatic interaction between cationic CV and $BaTiO_3$@ZnO composite. Subsequently, the composite was extracted from the solution, and the final pH of the solution was assessed.

3.2. Batch adsorption process

3.2.1. Effect of pH. The pH of the solution plays an essential role in the adsorption process because it affects the surface charge of the adsorbent, the ionization of the adsorbate molecules, and the interaction of the adsorbent with dye molecules.[36] The effect of pH on the removal efficiency of CV using either $BaTiO_3$ or $BaTiO_3$@ZnO composite was investigated by varying the pH range from 2 to 10 using 0.1 mol L^{-1} NaOH or 0.1 mol L^{-1} HCl and under consistent experimental conditions (initial dye concentration: 50 mg L^{-1}, adsorbent dose: 10 mg, dye volume: 10 mL, temperature: 35 °C, contact time: 360 min). As illustrated in Fig. 5a, the $BaTiO_3$ powder showed a gradual increase in the removal efficiency from 20.28% at pH 2 to 43.91% at pH 8–10. In comparison, the $BaTiO_3$@ZnO composite exhibited considerably higher performance; the removal efficiency increased from 32.07% at pH 2 to 86.91% at pH 6, after which it plateaued up to pH 10. The removal efficiency increases with increasing pH; this may be due to the reduction of the competition effect between H^+ ions and dye molecules for surface sites. Furthermore, the deprotonation of adsorbent surfaces supports the electrostatic attraction between the negatively charged surface and the cationic CV.[37] The removal efficiency reached a plateau at pH from neutral to alkaline; this suggests the saturation of the active site on the surface or the adsorption capacity became limited beyond a specific pH. The better efficiency of the composite is ascribed to the synergistic interaction between $BaTiO_3$ and ZnO, which improves surface charge distribution and enhances active sites for CV adsorption.

3.2.2. Influence of initial concentration of dye. The concentration of CV affects the adsorption efficiency of $BaTiO_3$ and $BaTiO_3$@ZnO composite. The experiment was performed in the range of initial concentration (30–200 mg L^{-1}); other parameters were kept constant (adsorbent dosage: 10 mg, solution volume: 10 mL, contact time: 360 min, temperature: 35 °C, pH: 8). The adsorption capacity (q_e) of both adsorbents rises with increasing dye concentration, as displayed in Fig. 5b. The $BaTiO_3$@ZnO composite showed higher adsorption capacity than $BaTiO_3$. The composite displayed a maximum q_e of ~91.6 mg g^{-1} at (150–200) mg L^{-1}. The $BaTiO_3$ showed a maximum q_e of ~22 mg g^{-1} at 50 mg L^{-1}. The superior efficiency of the composite is attributed to the synergistic effect between ZnO and $BaTiO_3$, which increases surface area, improves porosity, and boosts electrostatic attraction and

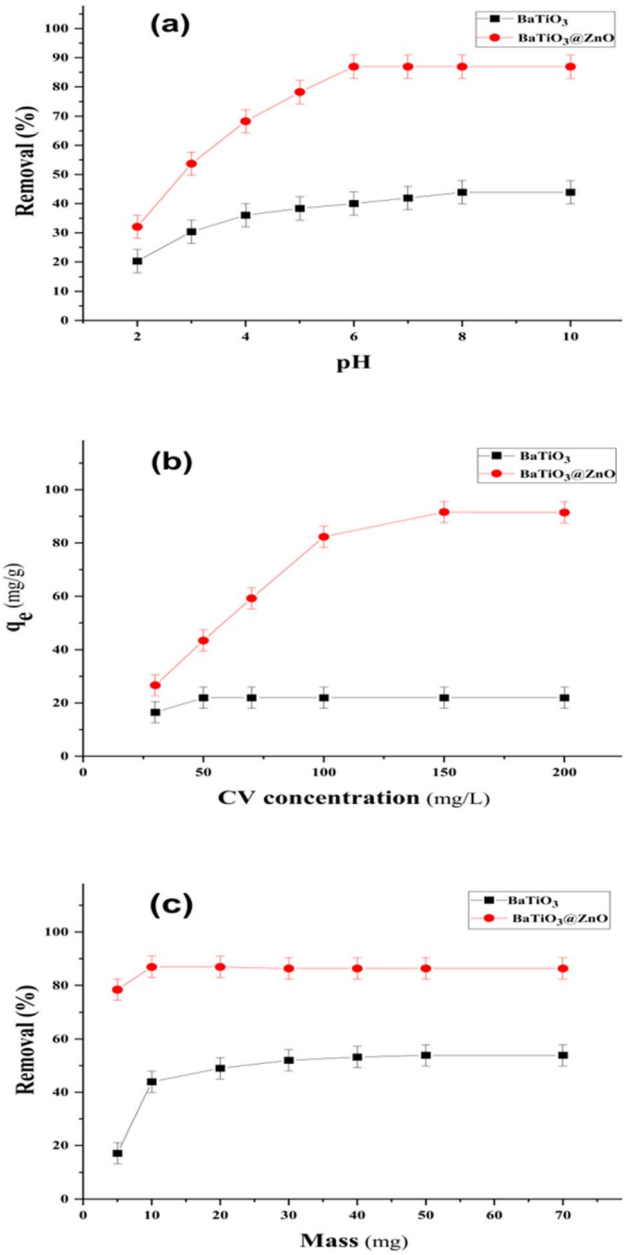

Fig. 5 (a) Effect of pH; (b) influence of initial dye concentration; (c) influence of adsorbent dosage: on the removal and adsorption of CV using $BaTiO_3$@ZnO composite and $BaTiO_3$ (conditions: initial dye concentration = 50 mg L^{-1}, adsorbent dose = 10 mg, volume = 10 mL, temperature = 35 °C, equilibrium time = 360 min, pH = 8).

surface charge interaction with dye molecules. The results matched with other previous studies, which mentioned the advantages of composite oxide materials in improving adsorption capacity.[16]

3.2.3. Influence of adsorbent dosage. The adsorbent dose is an essential factor that influences dye removal performance by controlling the availability of active surface sites for adsorption. Under controlled conditions (an initial dye concentration of 50 mg L^{-1}, a solution volume of 10 mL, a temperature of 35 °C, a contact time of 360 min, and a pH of 8), the influence of the dosage of $BaTiO_3$ and $BaTiO_3$@ZnO composite on CV uptake was evaluated. The behavior of adsorption of the two adsorbents is different, as shown in Fig. 5c.

For $BaTiO_3$, a continual increase in dye removal was observed as the dose of the adsorbent was increased, showing better availability of binding sites.[38] At a specific dosage (approximately 50 mg), additional increments in dosage did not lead to a proportional enhancement in efficiency. The plateau behavior suggests that either too much adsorbent caused particle aggregation, which reduces the effective surface area

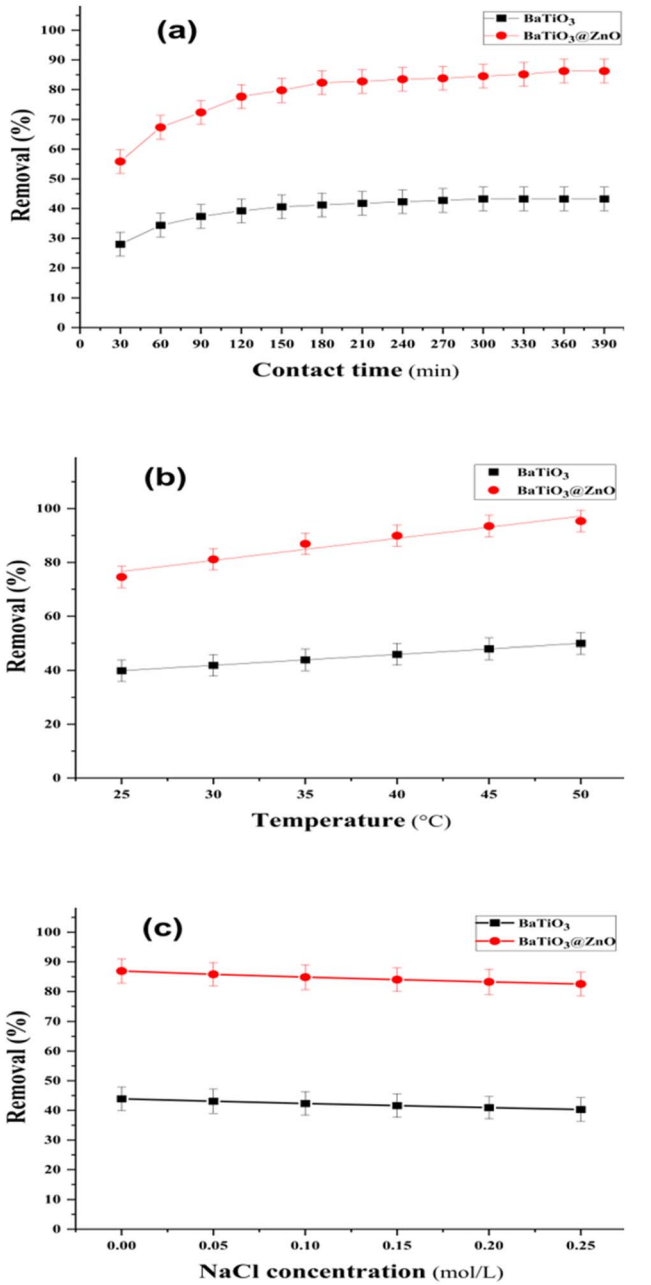

Fig. 6 (a) Influence of contact time; (b) influence of temperature; (c) influence of ionic strength: on the removal % of CV using $BaTiO_3$@ZnO composite and $BaTiO_3$ (conditions: initial dye concentration = 50 mg L^{-1}, adsorbent dose = 10 mg, volume = 10 mL, temperature = 35 °C, pH = 8, equilibrium time = 360 min).

and prevents more adsorption, or that the dye molecules were practically exhausted from the solution.[39]

The $BaTiO_3$@ZnO composite eliminated a substantial amount of the dye even at very low doses, with efficiency reaching its peak at about 10 mg. After that, as the dosage was increased, the performance was almost constant, suggesting that the adsorption sites were quickly saturated.[40] This enhancement can be explained by a synergistic effect between ZnO and $BaTiO_3$, which leads to an increment in the number of active sites, improves surface charge, and accelerates dye–adsorbent interactions. The removal capacity of the composite is high at low doses, which leads to savings in material and cost in water treatment processes.

3.2.4. Influence of contact time. Contact time is an essential parameter in the adsorption process and tells us how long the adsorption process takes to reach equilibrium. The effect of contact time on the removal of CV using $BaTiO_3$ and $BaTiO_3$@ZnO composite was investigated with different time intervals (30–390 min) at fixed experimental conditions: initial CV concentration of 50 mg L^{-1}, adsorbent dose of 10 mg, solution volume of 10 mL, temperature of 35 °C, and pH 8.

As shown in Fig. 6a, the $BaTiO_3$ exhibited a gradual increase of CV removal with time until reaching equilibrium at 300 min with a removal percent near 43%. The $BaTiO_3$@ZnO composite showed a more efficient adsorption process through a rapid CV uptake in the initial stage of contact time and a higher dye removal exceeding 86% at equilibrium time (360 min). The initial uptake of dye is rapid due to the presence of abundant active sites; with time, the saturation takes place, and the adsorption kinetics become slower.[41] The better performance of the composite is due to the synergistic effect between ZnO and $BaTiO_3$.

3.2.5. Influence of temperature. The temperature is a vital parameter in the adsorption process due to its effect on the surface characteristics of the adsorbent and the mobility of dye molecules in aqueous solutions. The influence of temperature on the removal efficiency of CV using $BaTiO_3$ and $BaTiO_3$@ZnO composite was examined at various temperatures of 25, 30, 35, 40, 45, and 50 °C under optimal conditions (10 mg of adsorbent to 10 mL of dye solution at an initial dye concentration of 50 mg L^{-1} and pH = 8 during an equilibrium time of 360 min). Fig. 6b illustrates that there is a steady increase in the removal efficiency as the temperature increases for both adsorbents, which suggests the adsorption of CV is temperature dependent. $BaTiO_3$ showed a gradual rise in the removal efficiency from 39.89% to 49.94% at 25 °C and 50 °C, respectively. The $BaTiO_3$@ZnO composite illustrated greater removal efficiency, which increased from 74.60% to 95.37% across the same temperature range. The enhancement of removal efficiency as a result of increasing temperature may be due to increased mobility, kinetic energy, and diffusion rate of dye molecules that become more accessible to the surface of the adsorbent.[42]

3.2.6. Influence of ionic strength. The effect of ionic strength on the adsorption of CV by $BaTiO_3$ and $BaTiO_3$@ZnO composite was analyzed using different concentrations of NaCl (0.05–0.25 mol L^{-1}) at fixed experimental conditions (C_0 = 50 mg L^{-1}, adsorbent dose = 10 mg, a solution volume = 10 mL, pH = 8, temperature = 35 °C, equilibrium time = 360 min). As exhibited in Fig. 6c, both adsorbents showed a gradual decrease in the removal efficiency of dye with increasing ionic strength. The reason may be related to the presence of excess Na^+ and Cl^- ions in the solution, which may compete with dye molecules for adsorption sites and compress the electrical double layer, leading to a decrease in the electrostatic attraction between the positively charged dye and the negatively charged surfaces of the adsorbent.

The $BaTiO_3$ displayed a small decrease in removal efficiency throughout the ionic strength range from 43.09% to 40.30%, which indicates restricted surface area and electrostatic interactions. While the $BaTiO_3$@ZnO composite showed improved and consistent removal efficiency, even at high salt concentrations, from 85.81% to 82.53%. This indicates increased surface reactivity and adsorption capacity. The results agree with earlier research, which suggests that the higher ionic strength might reduce dye adsorption. This happens due to charge screening and ion competition.[43]

3.2.7. Adsorption kinetics. Adsorption kinetics provides a critical understanding of the mechanism and rate of dye adsorption onto solid surfaces. Kinetics data are used in designing water treatment facilities. The kinetic behavior of CV adsorption onto $BaTiO_3$ and $BaTiO_3$@ZnO composite was examined in this research using three common models: pseudo-first-order, pseudo-second-order, and intra-particle diffusion models.

3.2.7.1. Pseudo-first-order kinetics. The pseudo-first-order model, as proposed by Lagergren, is that the rate of dye adsorption is directly proportional to the quantity of unoccupied adsorption sites.[44] The linearized model is expressed as

$$\log(q_e - q_t) = \log q_e - \left(\frac{k_1}{2.303}\right)t \quad (5)$$

where q_e and q_t (both in mg g^{-1}) are, respectively, the adsorbed amounts at equilibrium and at time t, and k_1 (min^{-1}) is the equilibrium rate constant for the pseudo-first-order adsorption. The magnitudes of k_1 and q_e were measured from the slope and intercept of the linear plot of $\log(q_e–q_t)$ against t (Fig. 7a). Although the correlation coefficients are high in this model (R^2 = 0.9861 for $BaTiO_3$ and 0.9582 for $BaTiO_3$@ZnO), the calculated q_e values were far from the experimental values, suggesting that the pseudo-first-order model is incapable of describing the adsorption mechanism. This reveals that physical adsorption is not the rate-controlling force in adsorption.

3.2.7.2. Pseudo-second-order kinetics. The pseudo-second-order model suggests that the rate of adsorption is governed by chemisorption, which is referred to as the sharing or exchange of electrons between adsorbate and adsorbent.[45] Its linear form is

$$\frac{t}{q_t} = \frac{1}{k_2 q_e^2} + \frac{t}{q_e} \quad (6)$$

where k_2 (g mg^{-1} min) is the equilibrium rate constant of the pseudo-second-order adsorption, and q_e was calculated from the plot of $\frac{t}{q_t}$ *versus* t (Fig. 7b).

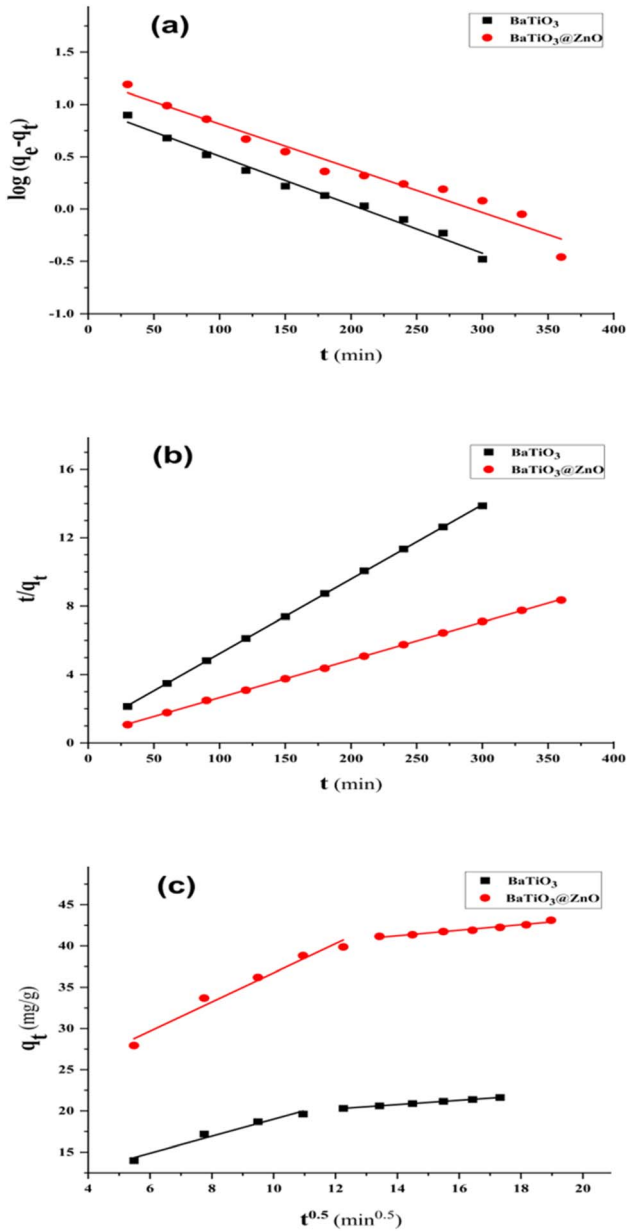

Fig. 7 (a) Pseudo-first-order kinetic model; (b) pseudo-second-order kinetic model; (c) intra-particle diffusion model: for adsorption of CV onto $BaTiO_3$@ZnO composite and $BaTiO_3$.

This model perfectly correlated with experimental data for both adsorbents, presenting correlation coefficients of $R^2 = 0.9998$ for the $BaTiO_3$@ZnO composite and $R^2 = 0.9999$ for $BaTiO_3$. Additionally, the calculated equilibrium capacities were very similar to the experimental values, showing that chemical interactions control the adsorption process.

3.2.7.3. Intraparticle diffusion model. Weber and Morris introduced the intra-particle diffusion model to examine the influence of pore diffusion on adsorption kinetics.[46] The equation can be expressed as

$$q_t = k_{id}t^{1/2} + C_i \quad (7)$$

where q_t (mg g^{-1}) is the adsorption capacity at time t (min), k_{id} (mg g^{-1} $min^{-0.5}$) is the intra-particle diffusion constant, and C_i is the intercept at stage i and represents boundary layer thickness. k_{id} and C_i were computed from the (q_t against $t^{1/2}$) plot (Fig. 7c). The plots showed multi-stage linearity, indicating that the adsorption process was divided into two stages: an initial external surface adsorption and intra-particle diffusion. The plots did not pass through the origin, suggesting that intra-particle diffusion was not the only rate-controlling mechanism. Compared to $BaTiO_3$ alone, the $BaTiO_3$@ZnO composite showed superior surface accessibility and diffusion properties, as evidenced by its higher k_{id} values.

In summary, among the three kinetic models studied, the pseudo-second-order model most accurately supplied the adsorption kinetics of CV on both $BaTiO_3$ and $BaTiO_3$@ZnO composite, pointing to chemisorption as the predominant mechanism. The enhanced performance of the composite is mainly due to the synergistic interaction between $BaTiO_3$ and ZnO, which resulted in increased surface activity and faster dye uptake. Table 4 summarizes the adsorption parameters for the kinetic models.

3.2.8. Adsorption isotherms. Adsorption isotherms are mathematical models that define the relation between the amount of adsorbate adsorbed on the surface of the adsorbent and the concentration of adsorbate in solution at equilibrium. Adsorption isotherms are necessary to understand the adsorption mechanism. Three classical isotherms for the equilibrium modeling of data, including the Langmuir, Freundlich, and Temkin isotherms, were employed in this work.

3.2.8.1. Langmuir isotherm. According to the Langmuir theory, monolayer adsorption takes place on a surface with a finite number of identical sites.[47] Its linear approximation is given by eqn (8)

$$\frac{C_e}{q_e} = \frac{1}{bq_m} + \frac{1}{q_m}C_e \quad (8)$$

where C_e (mg L^{-1}) is the equilibrium concentration of dye, q_e (mg g^{-1}) is the amount of dye adsorbed at the equilibrium, b (L mg^{-1}) is the Langmuir isotherm constant representing the affinity of binding sites, and q_m (mg g^{-1}) is the monolayer adsorption capacity. The slope and interception of the linear curve of C_e/q_e against C_e (Fig. 8a) are used to determine the values of q_m and b, respectively, and are reported in Table 5. Also, the coefficient of correlation (R^2) is determined. Moreover, this model yields a dimensionless separation factor, R_L, to indicate the favorability of adsorption. It can be stated as

$$R_L = \frac{1}{1 + bC_0} \quad (9)$$

where b (L mg^{-1}) is the Langmuir isotherm constant and C_0 (mg L^{-1}) is the maximum initial dye concentration. When the value of R_L is between 0 and 1, it would indicate favorable adsorption conditions.[48]

3.2.8.2. Freundlich isotherm. The Freundlich isotherm is an empirical model that incorporates multilayer adsorption and heterogeneous surface energies.[49] It can be expressed with the linearized formula

Table 4 Adsorption parameters for kinetic studies

	$BaTiO_3$		$BaTiO_3$@ZnO composite	
Kinetic model	Parameters	Values	Parameters	Values
Pseudo first order	q_e exp (mg g^{-1})	21.96	q_e exp (mg g^{-1})	43.46
	R^2	0.9861	R^2	0.9582
	q_e calc (mg g^{-1})	9.34	q_e calc (mg g^{-1})	17.28
	k_1 (min^{-1})	10.7×10^{-3}	k_1 (min^{-1})	9.76×10^{-3}
Pseudo second order	R^2	0.9999	R^2	0.9998
	q_e calc (mg g^{-1})	22.98	q_e calc (mg g^{-1})	45.26
	k_2 (g mg^{-1} min^{-1})	21.43×10^{-4}	k_2 (g mg^{-1} min^{-1})	10.95×10^{-4}
Intra particle diffusion	R^2	0.9537	R^2	0.9629
	K_{1D} (mg g^{-1} $min^{-0.5}$)	1.03	K_{1D} (mg g^{-1} $min^{-0.5}$)	1.77
	C_1 (mg g^{-1})	8.70	C_1 (mg g^{-1})	19.08
	R^2	0.9995	R^2	0.9585
	K_{2D} (mg g^{-1} $min^{-0.5}$)	0.261	K_{2D} (mg g^{-1} $min^{-0.5}$)	0.336
	C_2 (mg g^{-1})	17.10	C_2 (mg g^{-1})	36.52

$$\ln q_e = \ln K_f + \frac{1}{n} \ln C_e \quad (10)$$

where K_f is the Freundlich constant for the adsorption capacity, and $1/n$ is a heterogeneity factor. The magnitudes of the K_f and n were estimated from the intercept and slope of the linear plot of $\ln q_e$ against $\ln C_e$ (Fig. 8b), respectively, and are shown in Table 5. The correlation coefficient (R^2) is also presented. A $1/n < 1$ suggests favorable adsorption and higher interactions at lower concentrations.

3.2.8.3. Temkin isotherm. The Temkin isotherm considers the effect of indirect adsorbate–adsorbate interactions on adsorption heat. It assumes that the adsorption energy decreases linearly with increasing surface coverage.[50] The linear equation is

$$q_e = \frac{RT}{b_T} \ln K_T + \frac{RT}{b_T} \ln C_e \quad (11)$$

Here, R is the universal gas constant, T is the temperature, b_T (J mol^{-1}) is the Temkin constant associated with the heat of adsorption, and K_T (L g^{-1}) is the Temkin binding energy constant. b_T and K_T can be estimated from the slope and intercept of the plot of q_e against $\ln C_e$ (Fig. 8c), respectively, and are displayed in Table 5. Also, the correlation coefficient (R^2) is depicted.

According to the experimental data, the adsorption of CV on $BaTiO_3$ and $BaTiO_3$@ZnO composite was found to be most appropriately fitted by the Langmuir model, with the highest correlation coefficients ($R^2 > 0.996$), and the maximum adsorption capacities for both adsorbents are in close agreement with the experimental values. This indicates monolayer adsorption on uniform surfaces. Supported by these results, the R_L values of $BaTiO_3$ and $BaTiO_3$@ZnO composite are both in the range from 0 to 1, suggesting that the adsorption of CV by $BaTiO_3$ and $BaTiO_3$@ZnO composite is favorable. The adsorption capacity increases to 97.84 mg g^{-1} in the case of the $BaTiO_3$@ZnO composite, compared with 23.49 mg g^{-1} of $BaTiO_3$. Despite the Freundlich and Temkin models providing good fits, the lower R^2 values indicate that the adsorption process is consistent with Langmuir assumptions. The results validate the improved efficacy of the composite in dye removal applications, which is attributed to increased active sites and better interaction energies.

3.2.9. Thermodynamic studies. The dsorption process of CV onto $BaTiO_3$ and $BaTiO_3$@ZnO composites was explained by a thermodynamic investigation based on van't Hoff analysis. Gibbs free energy change ($\Delta G°$), enthalpy change ($\Delta H°$), and entropy change ($\Delta S°$) were calculated to establish the feasibility and nature of adsorption.[51] The equilibrium constant (K_c) can be written as

$$K_C = q_e/C_e \quad (12)$$

where (q_e) is the amount of dye adsorbed per unit mass of adsorbent at equilibrium (mg g^{-1}) and (C_e) is the equilibrium concentration of dye in the solution (mg L^{-1}).

$$\Delta G = -RT \ln K_C \quad (13)$$

The eqn (12) was employed to obtain $\Delta G°$, where T is the temperature in Kelvin and R is the universal gas constant.

$$\ln K_C = -\frac{\Delta H°}{RT} + \frac{\Delta S°}{R} \quad (14)$$

From the slope and intercept of the $\ln K_c$ against $1/T$ plot (Fig. 9a) and based on the van't Hoff equation eqn (13), $\Delta H°$ and $\Delta S°$ were obtained, respectively.

The adsorption of $BaTiO_3$ and $BaTiO_3$@ZnO composite is spontaneous, with values of $\Delta G°$ being negative at all temperatures studied. The positive $\Delta H°$ values confirm the endothermic adsorption, and the $BaTiO_3$@ZnO composite showed a higher enthalpy, which indicates a stronger interaction with dyes. The positive values of ($\Delta S°$) indicate the increased disorder at the solid–liquid interface during the adsorption. The results confirm the thermodynamic and effectiveness benefits of the $BaTiO_3$@ZnO composite for dye elimination (Table 6).

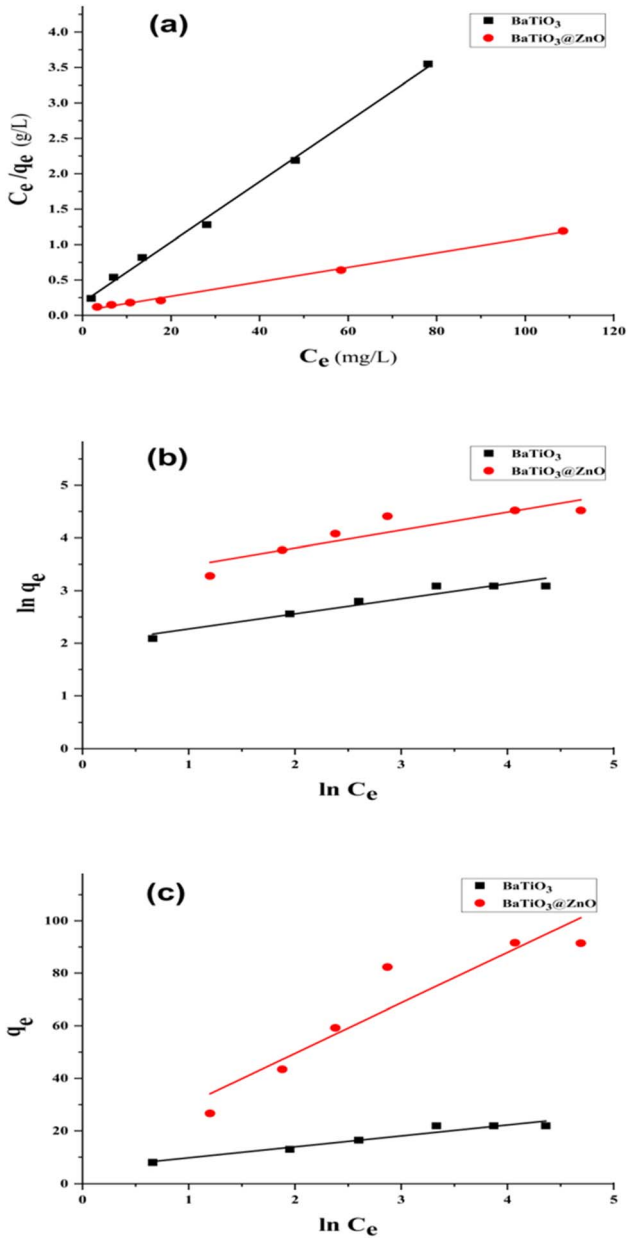

Fig. 8 (a) Langmuir plot; (b) Freundlich plot; (c) Temkin plot: for adsorption of CV onto $BaTiO_3$@ZnO composite and $BaTiO_3$.

Table 5 Isotherm parameters obtained for different models

	$BaTiO_3$		$BaTiO_3$@ZnO composite	
Isotherm	Parameters	Values	Parameters	Values
Experimental	q_{max} (mg g^{-1})	21.96	q_{max} (mg g^{-1})	91.60
Langmuir	R^2	0.9966	R^2	0.9961
	q_{max} (mg g^{-1})	23.49	q_{max} (mg g^{-1})	97.84
	b (L mg^{-1})	0.2309	b (L mg^{-1})	0.1559
	R_L	7.9×10^{-2}	R_L	4.1×10^{-2}
Freundlich	R^2	0.9141	R^2	0.7757
	K_f	7.27	K_f	22.86
	n	3.49	n	2.95
Temkin	R^2	0.9253	R^2	0.8520
	K_T (L g^{-1})	3.85	K_T (L g^{-1})	1.77
	b_T (J mol^{-1})	6.15×10^2	b_T (J mol^{-1})	1.33×10^2

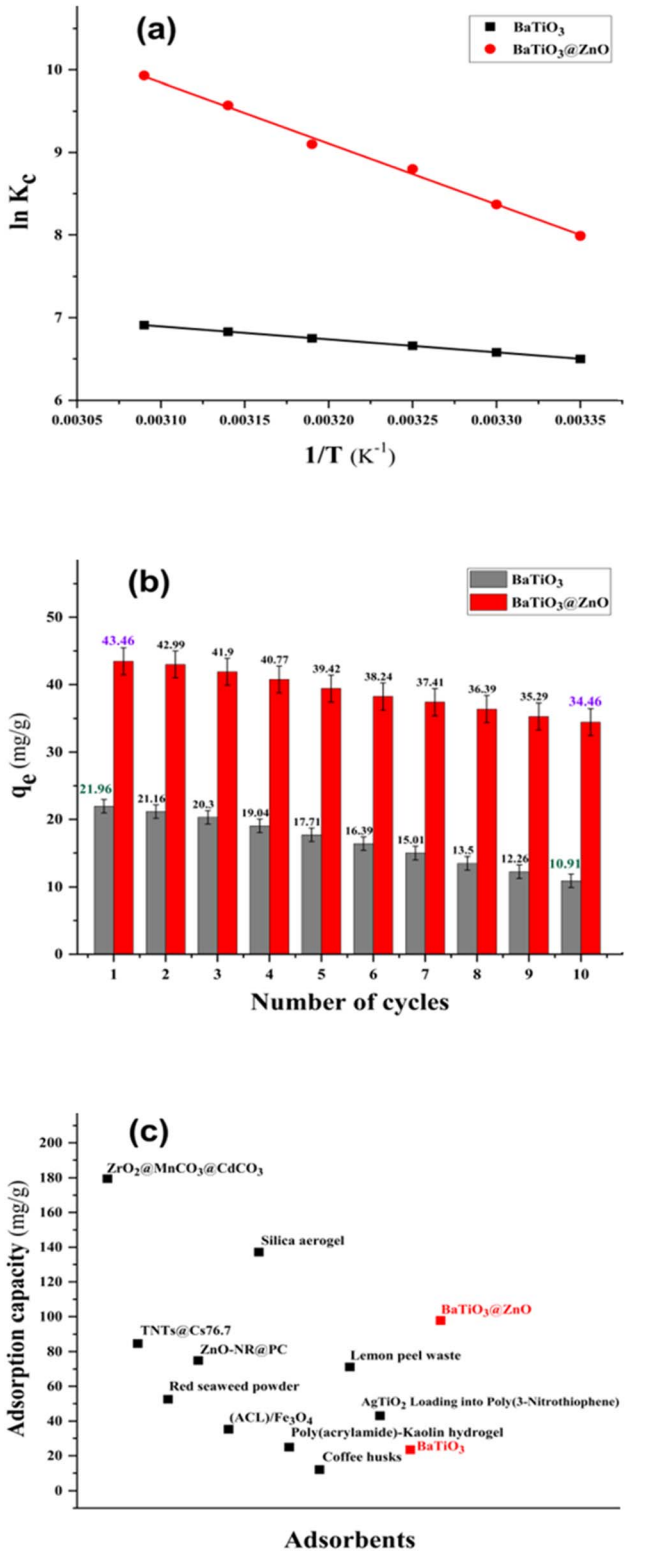

Fig. 9 (a) Van't Hoff plot for CV adsorption on $BaTiO_3$@ZnO composite and $BaTiO_3$; (b) adsorption of CV using the recycled adsorbents ($BaTiO_3$@ZnO composite and $BaTiO_3$) compared with a fresh one (conditions: initial dye concentration = 50 mg L^{-1}, adsorbent dose = 10 mg, volume = 10 mL, temperature = 35 °C, equilibrium time = 360 min, pH = 8); (c) Scatter plot comparing the maximum adsorption capacity of $BaTiO_3$@ZnO composite and $BaTiO_3$ with previously reported adsorbents for CV removal under various experimental conditions.

Table 6 Variables of thermodynamics at different temperatures

	$BaTiO_3$			$BaTiO_3$@ZnO composite		
T (K)	$\Delta G°$ (kJ mol^{-1})	$\Delta H°$ (kJ mol^{-1})	$\Delta S°$ (kJ mol^{-1} K^{-1})	$\Delta G°$ (kJ mol^{-1})	$\Delta H°$ (kJ mol^{-1})	$\Delta S°$ (kJ mol^{-1} K^{-1})
298	−16.106	13.06	0.0977	−19.793	61.36	0.272
303	−16.583			−21.090		
308	−17.070			−22.548		
313	−17.561			−23.689		
318	−18.055			−25.323		
323	−18.552			−26.687		

Table 7 Comparing adsorption capacity of $BaTiO_3$@ZnO composite and $BaTiO_3$ with other adsorbents

Adsorbent	q_m (mg g^{-1})	References
ZrO_2@$MnCO_3$@$CdCO_3$ nanocomposite	179.52	53
Chemically activated carbon spheres TNTs@Cs76.7	84.7	54
Red seaweed powder	52.6	55
ZnO-NR@PC-derived from orange peel	74.89	56
Activated carbon prepared from lemon wood (ACL)/Fe_3O_4 magnetic nanocomposite	35.3	57
Silica aerogel	137.17	58
Poly(acrylamide)-kaolin hydrogel	25.00	59
Coffee husks	12.04	60
Lemon peel waste	71.2	61
$AgTiO_2$ loading into poly(3-nitrothiophene)	43.10	62
ZnO	0.77	This work
$BaTiO_3$	23.49	This work
$BaTiO_3$@ZnO	97.84	This work

3.2.10. Desorption and reusability. As shown in Fig. 9b, the $BaTiO_3$@ZnO composite kept a good ability to remove dye, with the adsorption capacity going down from 43.46 mg g^{-1} in the first cycle to 34.46 mg g^{-1} in the tenth cycle, and the $BaTiO_3$ showed an obvious decrease from 21.96 to 10.91 mg g^{-1} for the same sequence. This indicates the potential of the $BaTiO_3$@ZnO composite as a more stable and recyclable adsorbent and the suitability of $BaTiO_3$@ZnO in the dye removal process. The retention of adsorption performance suggests good structural and chemical stability of the composite. In addition, the absence of significant performance degradation implies that Zn leaching is likely limited, which may be attributed to the strong interfacial interaction between $BaTiO_3$ and ZnO, as supported by the preserved crystalline features observed in XRD and FTIR analyses after reuse. These observations indicate that the composite exhibits considerable stability under repeated adsorption–desorption cycles.

3.2.11. Comparison with other adsorbents. Different adsorbents for CV and their adsorption capacities are exhibited in Table 7 and Fig. 9c. For comparison, the adsorption performance of unmodified ZnO toward CV was evaluated under identical experimental conditions. The results showed that unmodified ZnO exhibits a very low adsorption capacity (0.77 mg g^{-1}), which is mainly attributed to its restricted surface area and insufficient functional groups for effective interactions. Consequently, adsorption is negligible and predominantly confined to weak surface contacts rather than chemical bonding or pore entrapment.[52]

It is clear that the $BaTiO_3$@ZnO composite has a good maximum adsorption capacity (97.84 mg g^{-1}) compared to the others. This clearly demonstrates that the enhanced adsorption performance of the $BaTiO_3$@ZnO composite originates from the synergistic interaction between $BaTiO_3$ and ZnO rather than from ZnO alone. This comparison highlights the relevance of the present study and demonstrates the competitive performance of the $BaTiO_3$@ZnO composite for CV removal.

3.2.12. Application to real samples and economic considerations. To evaluate the method's efficiency and practicality for real samples, it was applied to remove and measure CV in different water samples, for example, Nile River water, sewage wastewater, and synthetic dye.[22] The samples were spiked with various concentrations of CV dye (5, 10, and 20 mg L^{-1} of dye) under optimum conditions (adsorbent dose: 10 mg, solution volume: 10 mL, pH: 8, contact time: 360 min, and temperature: 35 °C). As demonstrated in Table 8, the $BaTiO_3$@ZnO composite achieved a recovery percentage between 86.7% and 94.8% with a relative standard deviation (RSD%) of 1.27–2.70. While $BaTiO_3$ exhibited a recovery percentage ranging from 59.8% to 89.8% and RSD% from 1.53 to 2.88. The improved performance of $BaTiO_3$@ZnO is linked to its increased surface activity, whereas the slight reduction in complex water samples could be a result of competing ions and organic substances. The results confirm that the $BaTiO_3$@ZnO composite is suitable for treating real wastewater.

Table 8 Determination of CV in different real samples

		$BaTiO_3$			$BaTiO_3$@ZnO		
Sample	CV added (mg L^{-1})	CV found (mg L^{-1})	Recovery (%)	RSD[a] (%)	CV found (mg L^{-1})	Recovery (%)	RSD[a] (%)
Distilled water	—	—	—	—	—	—	—
	5	4.49	89.81	1.53	4.74	94.77	2.33
	10	8.07	80.72	2.22	9.30	92.98	1.93
	20	12.99	64.94	2.44	18.15	90.77	2.28
Synthetic dye	—	—	—	—	—	—	—
	5	4.45	88.98	2.17	4.70	93.94	2.35
	10	7.91	79.06	2.09	9.16	91.60	1.95
	20	12.75	63.73	2.27	17.91	89.53	2.46
Nile river water	—	—	—	—	—	—	—
	5	4.38	87.60	2.52	4.64	92.84	2.08
	10	7.78	77.78	2.36	9.06	90.63	2.58
	20	12.26	61.29	2.25	17.59	87.95	1.72
Sewage wastewater	—	—	—	—	—	—	—
	5	4.31	86.23	2.56	4.59	91.74	2.70
	10	7.59	75.90	2.54	9.01	90.08	1.38
	20	11.96	59.78	2.88	17.34	86.71	1.27

[a] For RSD, ($n = 3$).

Although $BaTiO_3$ and ZnO are not traditionally low-cost adsorbents, the synthesis procedure presented in this study is a solvent-free solid-state route that eliminates organic solvents, surfactants, or complex post-treatment steps. This significantly reduces material and operational costs. The synthesis also employs commercially available precursors, enabling large-scale production. The energy consumption in synthesis can also be minimized by controlling calcination temperature or using other low-energy techniques such as microwave-assisted, mechanochemical, and hydrothermal methods, which are claimed to reduce the synthesis temperatures while maintaining material performance. The higher adsorption efficiency, chemical stability, and reusability of the $BaTiO_3$@ZnO composite make it a good candidate for wastewater treatment applications, where regeneration and durability are critical.

3.2.13. Probable adsorption mechanism. The interaction mechanism between CV and the $BaTiO_3$@ZnO composite may be a mix of chemisorption and electrostatic interactions

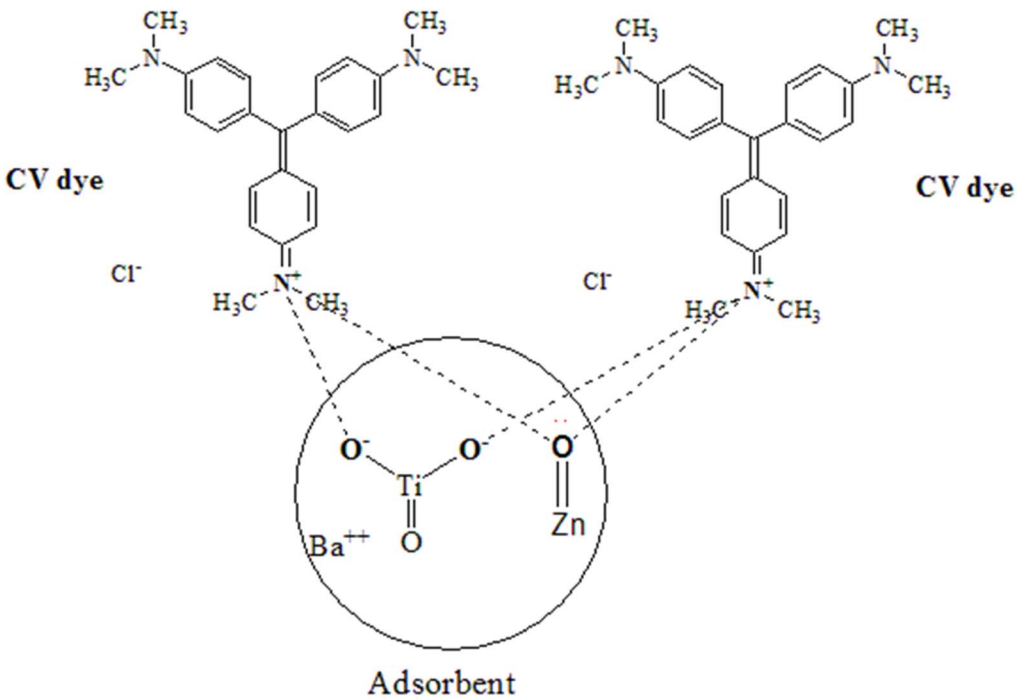

Fig. 10 adsorption mechanism of CV onto $BaTiO_3$@ZnO composite.

(Fig. 10). FTIR analysis and kinetic data suggest that chemisorption takes place. The Langmuir isotherm shows that monolayer adsorption occurs on a uniform surface. The thermodynamic study points out that the process is spontaneous and endothermic, which indicates a strong interaction between the dye and the adsorbent. ZnO improves the surface properties of $BaTiO_3$ by increasing the number of active sites and boosting the interaction with the positively charged dye molecules. The adsorption of CV onto $BaTiO_3$@ZnO is done through chemical bonding, surface attraction, and better surface activity. The $BaTiO_3$@ZnO composite is an efficient adsorbent for eliminating CV from wastewater.

From a mechanistic perspective, the adsorption of crystal violet onto the $BaTiO_3$@ZnO composite can be further described as a multistep process involving initial surface interactions followed by diffusion-controlled transport. Surface charge plays a critical role during the early stage of adsorption, where electrostatic attraction between the positively charged CV molecules and negatively charged surface sites of the composite facilitates rapid dye uptake. This electrostatic contribution is inherently dependent on solution pH and enhances the accessibility of available active sites. In addition to electrostatic interactions, possible chemical interactions between surface functional groups and dye molecules contribute to the overall adsorption mechanism, as inferred from FTIR spectral features and kinetic behavior. The incorporation of ZnO influences the interfacial properties of the composite by increasing surface heterogeneity and modifying charge distribution, thereby strengthening adsorbent–adsorbate interactions relative to pure $BaTiO_3$. Furthermore, diffusion pathways also play a role in governing the adsorption kinetics. The contact-time-dependent adsorption behavior suggests the involvement of both surface adsorption and intraparticle diffusion in controlling the overall uptake rate of CV molecules. It should be emphasized that the proposed adsorption mechanism is inferred from correlative experimental observations rather than directly validated by advanced surface-sensitive techniques such as XPS, zeta potential measurements as a function of pH, or SEM-EDX elemental mapping.

4. Conclusion

In this study, the $BaTiO_3$@ZnO composite was easily prepared and adopted as an adsorbent to remove CV from an aqueous solution. The characterization of the $BaTiO_3$@ZnO composite was executed using XRD, FTIR, SEM-EDX, TEM, BET, and pH_{ZPC}. The experimental factors, such as pH, initial dye concentration, adsorbent dosage, contact time, temperature, and ionic strength, influence the adsorption of CV onto $BaTiO_3$ and $BaTiO_3$@ZnO composite. The maximum adsorption capacity of $BaTiO_3$ and $BaTiO_3$@ZnO composite can attain 23.49 and 97.84 mg g^{-1}, respectively. Both adsorbents obeyed the Langmuir isotherm and the pseudo-second-order kinetic model, which demonstrated monolayer coverage on the surface and chemisorption as the main mechanism. Thermodynamic results suggest that the adsorption of CV onto $BaTiO_3$ and the $BaTiO_3$@ZnO composite was endothermic, spontaneous, and feasible. Both adsorbents can be recycled and reused for up to ten consecutive cycles, showing a gradual decrease in adsorption performance. The results confirmed that the $BaTiO_3$@ZnO composite is better and more effective than $BaTiO_3$ due to the addition of ZnO to $BaTiO_3$, which enhances surface area and porosity and facilitates the electrostatic attraction with CV molecules. The $BaTiO_3$@ZnO composite is an eco-friendly and inexpensive adsorbent and has potential for the remediation of wastewater contaminated with dyes. Further investigations using advanced surface characterization techniques are required to provide direct evidence of interfacial bonding and electrostatic contributions in the $BaTiO_3$@ZnO composite, and future work needs to study another metal oxide with $BaTiO_3$ or add a third ingredient to the composite for the elimination of cationic dyes from aqueous solution.

Author contribution

Ahmed Barakat: data curation, investigation, methodology, writing – original draft. Magdi E. Khalifa: conceptualization, data curation, investigation, methodology, supervision, writing – review & editing. A. M. Abdelghany: data curation, investigation, methodology and reviewing. Wael I. Mortada: conceptualization, data curation, investigation, methodology, supervision, writing – review & editing.

Conflicts of interest

The authors declare no competing interests.

Data availability

Data supporting this study are included within the article.

References

1 A. P. Periyasamy, Textile Dyes in Wastewater and its Impact on Human and Environment: Focus on Bioremediation, *Water, Air, Soil Pollut.*, 2025, **236**, 562.
2 C. R. S. de Oliveira, P. V. de Oliveira, G. C. O. de Aguiar, M. E. P. Missner, R. K. Tewo, A. H. da Silva Júnior, A. B. Mapossa and C. R. L. de Aguiar, Dyes and Dyeing of Textiles: An Overview of Sustainability Issues, *Sustainable Coloration Techniques in Textiles*, 2025, 1–54.
3 T. Islam, M. R. Repon, T. Islam, Z. Sarwar and M. M. Rahman, Impact of textile dyes on health and ecosystem: a review of structure, causes, and potential solutions, *Environ. Sci. Pollut. Res.*, 2023, **30**, 9207–9242.
4 N. Sen, N. R. Shefa, K. Reza, S. M. A. Z. Shawon and M. W. Rahman, Adsorption of crystal violet dye from synthetic wastewater by ball-milled royal palm leaf sheath, *Sci. Rep.*, 2024, **14**, 5349.
5 F. Le Curieux, J. M. Gohlke, A. Pronk, W. C. Andersen, G. Chen, J.-L. Fang, K. Mitrowska, P. J. Sanders, M. Sun and G. A. Umbuzeiro, Carcinogenicity of gentian violet, leucogentian violet, malachite green, leucomalachite green, and CI Direct Blue 218, *Lancet Oncol.*, 2021, **22**, 585–586.

6 S. Mani and R. N. Bharagava, Exposure to crystal violet, its toxic, genotoxic and carcinogenic effects on environment and its degradation and detoxification for environmental safety, *Rev. Environ. Contam. Toxicol.*, 2016, **237**, 71–104.
7 S. Ihaddaden, D. Aberkane, A. Boukerroui and D. Robert, Removal of methylene blue (basic dye) by coagulation-flocculation with biomaterials (bentonite and Opuntia ficus indica), *J. Water Proc. Eng.*, 2022, **49**, 102952.
8 X. Liu, M. Huang, S. Yang, R. Devasenathipathy, L. Xie, Z. Yang, L. Wang, D. Huang, X. Peng and D. H. Chen, Spatially Confined Radical Addition Reaction for Electrochemical Synthesis of Carboxylated Graphene and its Applications in Water Desalination and Splitting, *Small*, 2024, **20**, 2401972.
9 X. Liu, S. Yang, M. Huang, R. Devasenathipathy, Q. Huang, D. Huang, Z. Yang, L. Wang, D. H. Chen and J. F. Li, Spatially Confined Electrosynthesis of Halogen-Poor and Carbonyl-Rich Graphene for Boosting Water Desalination and Water Splitting, *Small Methods*, 2025, **9**, 2401591.
10 H. Heryanto and D. Tahir, Trends, mechanisms, and the role of advanced oxidation processes in mitigating azo, triarylmethane, and anthraquinone dye pollution: A bibliometric analysis, *Inorg. Chem. Commun.*, 2025, 114104.
11 Z. Huang, X. Zhang, F. Yang, R. Devasenathipathy, X. Peng, L. Wang, D. Huang, Y. Fan, W. Chen and D.-H. Chen, Strengthening cationic repulsion on graphene oxide membrane to boost water desalination, *J. Taiwan Inst. Chem. Eng.*, 2024, **165**, 105799.
12 B. Balachandran and P. Sabumon, A comprehensive review on biodegradation of Azo dye mixtures, metabolite profiling with health implications and removal strategies, *J. Hazard. Mater. Adv.*, 2025, 100834.
13 S. Sudarsan, G. Murugesan, T. Varadavenkatesan, R. Vinayagam and R. Selvaraj, Efficient adsorptive removal of Congo Red dye using activated carbon derived from Spathodea campanulata flowers, *Sci. Rep.*, 2025, **15**, 1831.
14 G. Bal and A. Thakur, Distinct approaches of removal of dyes from wastewater: A review, *Mater. Today: Proc.*, 2022, **50**, 1575–1579.
15 N. El Messaoudi, M. El Khomri, A. El Mouden, A. Bouich, A. Jada, A. Lacherai, H. M. Iqbal, S. I. Mulla, V. Kumar and J. H. P. Américo-Pinheiro, Regeneration and reusability of non-conventional low-cost adsorbents to remove dyes from wastewaters in multiple consecutive adsorption–desorption cycles: a review, *Biomass Convers. Biorefin.*, 2024, **14**, 11739–11756.
16 L. Wang, C. Shi, L. Pan, X. Zhang and J.-J. Zou, Rational design, synthesis, adsorption principles and applications of metal oxide adsorbents: a review, *Nanoscale*, 2020, **12**, 4790–4815.
17 S. K. Ray, J. Cho and J. Hur, A critical review on strategies for improving efficiency of BaTiO3-based photocatalysts for wastewater treatment, *J. Environ. Manage.*, 2021, **290**, 112679.
18 K. Nagaraja, B. Mallika, M. Arunpandian, E. Ravindran and O. T. Hwan, Green synthesis of gold-decorated BaTiO3-ZnO nanocomposites using Arabic gum polymer for efficient photocatalytic degradation of emerging textile dyes, antimicrobial, and toxicological evaluation, *Int. J. Biol. Macromol.*, 2025, **311**, 143396.
19 A. Brahimi, R. Chelghoum, J. P. Martínez Jiménez, N. Bourouba, N. Bouzit, A. yousfi, O. saidani and R. zerrougui, A Compact Cylindrical Dielectric Resonator Antenna Using (RE-BaTiO3-ZnO) for 5G Wireless Communication Applications, *ECS J. Solid State Sci. Technol.*, 2025, **14**(7), 073003.
20 A. Kholodkova, M. Danchevskaya, Y. D. Ivakin, A. Smirnov, S. Ponomarev, A. Fionov and V. Kolesov, Solid state synthesis of barium titanate in air and in supercritical water: Properties of powder and ceramics, *Ceram. Int.*, 2019, **45**, 23050–23060.
21 A. Barakat, W. I. Mortada, A. Abdelghany and M. E. Khalifa, Sustainable removal of malachite green from wastewater using mesoporous $BaTiO_3$: synthesis, characterization, and adsorption performance, *BMC Chem.*, 2025, **19**, 1–17.
22 L. Li, L. Yang, R. Zou, J. Lan, J. Shang, B. Dou, H. Liu and S. Lin, Facile and scalable preparation of ZIF-67 decorated cotton fibers as recoverable and efficient adsorbents for removal of malachite green, *J. Leather Sci. Eng.*, 2021, **3**, 28.
23 A. S. Ahmed, W. Xiang, I. S. Amiinu, Z. Li, R. Yu and X. Zhao, ZnO-nitrogen doped carbon derived from a zeolitic imidazolate framework as an efficient counter electrode in dye-sensitized solar cells, *Sustainable Energy Fuels*, 2019, **3**, 1976–1987.
24 H. Sellami, M. O. Akinyemi, M. Gdoura-Ben Amor, D. C. Onwudiwe and D. Mthiyane, Structural and optical characterization of TiO_2 nanoparticles synthesized using Globularia alypum leaf extract and the antibacterial properties, *Discover Appl. Sci.*, 2025, **7**, 1–19.
25 D. Padalia, U. Kumar, P. Bhandari, J. Dalal, L. Ranakoti and T. Singh, Tuning the structural, optical, and dielectric properties of europium-doped barium titanate ceramics, *J. Mater. Sci.: Mater. Electron.*, 2024, **35**, 1375.
26 M. Singh, B. Yadav, A. Ranjan, M. Kaur and S. Gupta, Synthesis and characterization of perovskite barium titanate thin film and its application as LPG sensor, *Sens. Actuators, B*, 2017, **241**, 1170–1178.
27 P. G. Devi and A. S. Velu, Synthesis, structural and optical properties of pure ZnO and Co doped ZnO nanoparticles prepared by the co-precipitation method, *J. Theor. Appl. Phys.*, 2016, **10**, 233–240.
28 R. Bayat, E. Halvaci, M. Bekmezci, G. Kaya, H. B. Poyraz, I. Kaynak and F. Sen, Production of boron nitride/titanium dioxide composite nanofibers *via* sustainable electrospinning methods and their environmentally friendly photocatalytic and antibacterial applications, *RSC Adv.*, 2025, **15**, 18648–18656.
29 B. Xu, A. Hirsch, L. Kronik and K. M. Poduska, Vibrational properties of isotopically enriched materials: the case of calcite, *RSC Adv.*, 2018, **8**, 33985–33992.
30 M. Adel, A. M. El Naggar, A. Bakry, M. H. Hilal, A. A. El-Zahhar, M. H. Taha and A. Marey, Decoration of polystyrene with nanoparticles of cobalt hydroxide as new composites for the removal of Fe (iii) and methylene blue

from industrial wastewater, *RSC Adv.*, 2023, **13**, 25334–25349.

31 M. Chitkara, N. Goyal, A. Kumar, L. Marasamy, S. Haq, S. A. Aldossari, R. Haldhar and M. K. Hossain, Tailoring graphene-oxide and reduced-graphene-oxide with NaNO 3 and CaCl 2 catalysts with enhanced photo-catalytic degradation of methylene blue dye, *RSC Adv.*, 2024, **14**, 8769–8778.

32 M. B. Nayan, K. Jagadish, M. R. Abhilash, K. Namratha and S. Srikantaswamy, Comparative study on the effects of surface area, conduction band and valence band positions on the photocatalytic activity of ZnO-M x O y heterostructures, *J. Water Resour. Prot.*, 2019, **11**, 357.

33 S.-H. Nam, S.-J. Cho and J.-H. Boo, Growth behavior of titanium dioxide thin films at different precursor temperatures, *Nanoscale Res. Lett.*, 2012, **7**, 89.

34 M. Ahamed and M. M. Khan, Enhanced photocatalytic and anticancer activity of Zn-doped BaTiO3 nanoparticles prepared through a green approach using Banana Peel extract, *Catalysts*, 2023, **13**, 985.

35 L. L. Borba, R. M. F. Cuba, F. J. C. Terán, M. N. Castro and T. A. Mendes, Use of adsorbent biochar from Pequi (Caryocar Brasiliense) husks for the removal of commercial formulation of glyphosate from aqueous media, *Braz. Arch. Biol. Technol.*, 2019, **62**, e19180450.

36 S. Wong, N. A. Ghafar, N. Ngadi, F. A. Razmi, I. M. Inuwa, R. Mat and N. A. S. Amin, Effective removal of anionic textile dyes using adsorbent synthesized from coffee waste, *Sci. Rep.*, 2020, **10**, 2928.

37 A. Tomczyk, Z. Sokołowska and P. Boguta, Biochar physicochemical properties: pyrolysis temperature and feedstock kind effects, *Rev. Environ. Sci. Bio/Technol.*, 2020, **19**, 191–215.

38 S. S. Metwally, R. S. Hassan, E. H. El-Masry and E. H. Borai, Gamma-induced radiation polymerization of kaolin composite for sorption of lanthanum, europium and uranium ions from low-grade monazite leachate, *J. Radioanal. Nucl. Chem.*, 2018, **315**, 39–49.

39 T. Laktif, A. Imgharn, A. Hsini, M. Elhoudi, N. Aarab, M. Laabd, R. Lakhmiri and A. Albourine, Sunflower seed shells@ polyaniline: a novel composite for the removal of pharmaceutical pollutants from wastewater, *Int. J. Environ. Anal. Chem.*, 2024, **104**, 2195–2212.

40 S. Natarajan, H. C. Bajaj and R. J. Tayade, Recent advances based on the synergetic effect of adsorption for removal of dyes from waste water using photocatalytic process, *J. Environ. Sci.*, 2018, **65**, 201–222.

41 D. D. Anuse, S. A. Patil, A. A. Chorumale, A. G. Kolekar, P. P. Bote, L. S. Walekar and S. P. Pawar, Activated carbon from pencil peel waste for effective removal of cationic crystal violet dye from aqueous solutions, *Results Chem.*, 2025, **13**, 101949.

42 F. S. Awad, K. M. AbouZied, W. M. Abou El-Maaty, A. M. El-Wakil and M. S. El-Shall, Effective removal of mercury (II) from aqueous solutions by chemically modified graphene oxide nanosheets, *Arabian J. Chem.*, 2020, **13**, 2659–2670.

43 B. Tanhaei, A. Ayati, E. Iakovleva and M. Sillanpää, Efficient carbon interlayed magnetic chitosan adsorbent for anionic dye removal: Synthesis, characterization and adsorption study, *Int. J. Biol. Macromol.*, 2020, **164**, 3621–3631.

44 A. N. Ebelegi, N. Ayawei and D. Wankasi, Interpretation of adsorption thermodynamics and kinetics, *Open J. Phys. Chem.*, 2020, **10**, 166–182.

45 M. Haerifar and S. Azizian, Mixed surface reaction and diffusion-controlled kinetic model for adsorption at the solid/solution interface, *J. Phys. Chem. C*, 2013, **117**, 8310–8317.

46 S. P. Dharmarathna and N. Priyantha, Investigation of boundary layer effect of intra-particle diffusion on methylene blue adsorption on activated carbon, *Energy Nexus*, 2024, **14**, 100294.

47 I. Langmuir, The adsorption of gases on plane surfaces of glass, mica and platinum, *J. Am. Chem. Soc.*, 1918, **40**, 1361–1403.

48 H. M. Marwani, H. M. Albishri, T. A. Jalal and E. M. Soliman, Study of isotherm and kinetic models of lanthanum adsorption on activated carbon loaded with recently synthesized Schiff's base, *Arabian J. Chem.*, 2017, **10**, S1032–S1040.

49 N. Ayawei, A. N. Ebelegi and D. Wankasi, Modelling and interpretation of adsorption isotherms, *J. Chem.*, 2017, **2017**, 3039817.

50 A. D. Khatibi, M. Yilmaz, A. H. Mahvi, D. Balarak and S. Salehi, Evaluation of surfactant-modified bentonite for Acid Red 88 dye adsorption in batch mode: Kinetic, equilibrium, and thermodynamic studies, *Desalination Water Treat.*, 2022, **271**, 48–57.

51 A. H. Jawad, A. S. Abdulhameed, S. Surip and S. Sabar, Adsorptive performance of carbon modified chitosan biopolymer for cationic dye removal: kinetic, isotherm, thermodynamic, and mechanism study, *Int. J. Environ. Anal. Chem.*, 2022, **102**, 6189–6203.

52 A. Marubini, R. Mhlarhi and J. N. Edokpayi, Adsorptive removal of crystal violet dye from aqueous solution using a vermiculite-based geopolymer, *Sci. Afr.*, 2025, **28**, e02701.

53 N. S. Al-Kadhi, E. A. Abdelrahman, F. S. Alamro, F. A. Saad and D. S. Al-Raimi, Innovative nanocomposite comprising of ZrO2, MnCO3, and CdCO3 for superior crystal violet dye adsorption: Synthesis, characterization, and regeneration insights, *Sci. Rep.*, 2025, **15**, 5525.

54 A. M. Mohammed, A. Kotb, M. M. Sanad, M. Abdel-Hakim and A. S. Ahmed, Enhanced adsorption of carbon sphere by doping with titania nanotubes for crystal violet removal: isotherm, kinetics, and thermodynamic studies, *RSC Adv.*, 2024, **14**, 31332–31347.

55 S. I. Al-Saeedi, M. Ashour and A. E. Alprol, Adsorption of toxic dye using red seaweeds from synthetic aqueous solution and its application to industrial wastewater effluents, *Front. Mar. Sci.*, 2023, **10**, 1202362.

56 E. J. Abdelrazek, A. A. Gahlan, G. A. Gouda and A. S. Ahmed, Cost-effective adsorption of cationic dyes using ZnO nanorods supported by orange peel-derived carbon, *Sci. Rep.*, 2025, **15**, 4123.

57 R. Foroutan, S. J. Peighambardoust, S. H. Peighambardoust, M. Pateiro and J. M. Lorenzo, Adsorption of crystal violet dye using activated carbon of lemon wood and activated carbon/Fe3O4 magnetic nanocomposite from aqueous solutions: a kinetic, equilibrium and thermodynamic study, *Molecules*, 2021, **26**, 2241.

58 S. Gupta, A. Prajapati, A. Kumar and S. Acharya, Synthesis of silica aerogel and its application for removal of crystal violet dye by adsorption, *Watershed Ecol. Environ.*, 2023, **5**, 241–254.

59 S. Shirsath, A. Patil, B. Bhanvase and S. Sonawane, Ultrasonically prepared poly (acrylamide)-kaolin composite hydrogel for removal of crystal violet dye from wastewater, *J. Environ. Chem. Eng.*, 2015, **3**, 1152–1162.

60 G. K. Cheruiyot, W. C. Wanyonyi, J. J. Kiplimo and E. N. Maina, Adsorption of toxic crystal violet dye using coffee husks: Equilibrium, kinetics and thermodynamics study, *Sci. Afr.*, 2019, **5**, e00116.

61 S. K. M. Rozi, K. Y. Qin, H. N. A. Halim, M. M. H. Al-Rajabi and A. R. Ishak, Green removal of toxic crystal violet using agricultural wastes: mechanisms, phytotoxicity, economic, and greenness profiling, *Biomass Convers. Biorefin.*, 2025, 1–19.

62 S. A. Alqarni, The performance of different AgTiO2 loading into poly (3-Nitrothiophene) for efficient adsorption of hazardous brilliant green and crystal violet dyes, *Int. J. Polym. Sci.*, 2022, **2022**, 4691347.